

MULTISCALE ANALYSIS OF ANISOTROPIC MATERIALS WITH HEXAGONAL MICROSTRUCTURE AS MICROPOLAR CONTINUA

N. Fantuzzi,^{1,*} P. Trovalusci,² & R. Luciano³

¹DICAM Department, University of Bologna, Viale del Risorgimento 2, 40136, Bologna, Italy

²DISG Department, Sapienza University of Rome, Via A. Gramsci, 53, 00197, Roma, Italy

³Engineering Department, Parthenope University, Centro Direzionale (Isola C4), 80133, Napoli, Italy

*Address all correspondence to: N. Fantuzzi, DICAM Department, University of Bologna, Viale del Risorgimento 2, 40136, Bologna, Italy, E-mail: nicholas.fantuzzi@unibo.it

Original Manuscript Submitted: 11/9/2019; Final Draft Received: 11/26/2019

This work discusses the advantages of micropolar theory in modeling anisotropic composite materials with microstructure. A homogenized constitutive model starting from a representative volume element is proposed in order to find an equivalent continuum. Classical (e.g., Cauchy of Grade 1) continua are not always suitable to accurately approximate the behavior of such composites because no size effects, nor lack of symmetries in strain and stress, can be taken into account. This study focuses on composites made of hexagonal rigid particles which interact among themselves through elastic interfaces, so that the deformation energy of the material is concentrated only at the interfaces. Three particle geometries are investigated such as orthotetragonal, auxetic, and chiral. Novel results have been achieved by presenting the behavior of panels with various material symmetries and subjected to concentrated loads.

KEY WORDS: multiscale, anisotropic materials, finite element method, Cosserat (micropolar), homogenization, RVE

1. INTRODUCTION

Composite materials can be studied by modeling interactions among their constituents or by homogenizing an equivalent continuum. The former approach generally requires higher computational cost because of the detailed modeling of particle/matrix interactions such as discrete element modeling (Baraldi et al., 2018; Reccia et al., 2018; Yang et al., 2010). The latter, as any field theory, is more efficient but its effectiveness is strongly related to the continuum theory used and the homogenization method adopted to convert the physical particle/matrix system into an equivalent continuum (e.g., Budiansky, 1965; Ehlers, 2011; Nemat-Nasser et al., 2013).

In order to model complex spatial interaction effects or describe materials in which internal length scales are not negligible when compared to structural length scales, homogenization techniques of different kind have also been extended to non-classical continua [see the review in Trovalusci (2014)]. This latter circumstance becomes significant when dealing with complex constitutive behaviors dependent on the microstructure size, such as strain localization, and the field equations of the simple (Grade 1) classical continuum become ill-posed. To this regard, some models including extra parameters, such as internal length, aiming to take into account the material nonlocality at the constitutive level only without modifying the classical kinematics have been proposed by Alibert and Della Corte (2015), Civalek et al. (2010), Demir and Civalek (2013), Larsson and Zhang (2007). Non-local or higher-order deformation gradient descriptions, specifically addressed to multiscale computational homogenization, have been also proposed by Bacigalupo and Gambarotta (2010), Kouznetsova et al. (2002, 2004), Leismann and Mahnken (2015), Massart et al. (2007), Peerlings and Fleck (2004), Sluys et al. (1993), as well as non-local explicit solutions obtained

for specific cases of elastic composites (Bacca et al., 2013; Drugan and Willis, 1996; Luciano and Willis, 2000; Smyslyayev and Cherednichenko, 2000). Within the framework of “implicit” non-local theories concerning models with additional degrees of freedom (Trovalusci, 2014; Tuna et al., 2019; Tuna and Trovalusci, 2020), micromorphic continua, in particular continua with rigid local structure (micropolar), have been satisfactorily applied to various composites (Addessi and Sacco, 2012; Bouyge et al., 2001; Forest et al., 1999, 2001; Forest and Sab, 1998; Masiani and Trovalusci, 1996; Onck, 2002; Ostoja-Starzewski et al., 1999; Tekolu and Onck, 2008; Trovalusci and Masiani, 2003, 2005; Trovalusci and Sansalone, 2007).

All the above-mentioned models can be defined as non-local as the field equations contain internal length parameters revealing the presence of a hidden microstructure which can affect the macroscopic behavior and there are dispersion properties in wave propagation (Kunin, 1968). Size effect on such non-local materials can be investigated as parametric simulations in order to better fit experimental evidences.

Homogenization-based techniques have been widely exploited to study material failure behavior. For instance Jain and Ghosh (2009) presented the damage evolution of composite materials via a Continuum Damage Mechanics Model. Altenbach and Sadowski (2014) worked on failure and damage analysis of advanced materials. Implementation and computational aspects of multiscaled cracked problems have been proposed by Nguyen et al. (2012). Collapse of three-dimensional systems made of blocks using a nonlinear implementation has been presented by Yang et al. (2000). Analogously, Greco et al. (2016, 2017, 2018) studied the effects of microfractures and contact simulations on the macroscopic response of elastic bodies in finite deformations and fiber-reinforced materials.

When classical kinematics is enriched with extra degrees of freedom, homogenization procedures have been shown to provide more reliable models than in the case of classical local continua, as for instance in the study of wave propagation within the framework of generalized continuum formulations for composite microcracked bars as reported by Trovalusci et al. (2010) or also in the study of multiphysics problems such as thermo-elastic multifield materials in Favata et al. (2016). In particular, micropolar theory introduces as degree of freedom the microrotation, that is, an additional kinematic feature of the material point, different from the local rigid rotation (the classical macrorotation), the rotational feature of the infinitesimal neighborhood, and their effects have been widely investigated by Fantuzzi et al. (2019), Pau and Trovalusci (2012), Trovalusci and Masiani (2003, 2005), Trovalusci and Pau (2014) for masonry-like materials. Note that these rotations coincide in the couple-stress theory, as well as in the classical theory [see Masiani and Trovalusci (1996), Appendix]. As it has been also recently analyzed by Fantuzzi et al. (2018), micropolar effects become prominent when geometrical or load singularities are present in the reference problem, such as concentrated loads, voids, or material inclusions and these effects have been also compared to those of other kinds of non-local continuum descriptions (Tuna et al., 2019; Tuna and Trovalusci, 2020).

The present work aims at presenting the mechanical micropolar behavior of hexagonal lattices (Rizzi et al., 2019; Trovalusci et al., 2017) with elastic interfaces. Different selections of hexagonal geometries and interface orientations lead to a distinct material symmetry (Eremeyev and Pietraszkiewicz, 2016). In the present work three assemblies are considered such as regular, hourglass, and chiral placement of the hexagonal particles which are all derived from a hexagonal pattern with sides of all the same lengths (equilateral). The first pattern regards regular hexagonal shapes having the orthotetragonal symmetry. The second is obtained from regular hexagons but with re-entrant corners; this give an hourglass shape and auxetic properties to the material due to an equivalent negative Poisson ratio. Finally, the third, is an asymmetric pattern given by one re-entrant corner and one not re-entrant starting from the regular shape. The equivalent continuum in this case results to be chiral, by coupling the classical part of stress/strain with micropolar couple stresses/curvatures. Novel results have been achieved by presenting the behavior of the aforementioned material configurations under concentrated loads.

This paper is structured as follows. First, the Cosserat continuum model is briefly presented in order to introduce current quantities and symbols. Second, a parametric hexagonal geometry based on four parameters is presented and the investigated patterns are shown and defined. Third, the present in-house finite element implementation is presented using linear finite elements with reduced integration. Finally, numerical applications are discussed by comparison among the three considered geometries and physical deduction from the contour plots are given.

2. MICROPOLAR CONTINUUM

In micropolar theory, the continuum considers the microrotation of the material particles which is added to the Cartesian displacements. The material particle of a micropolar continuum experiences displacements and rotations; in a 3D framework there are three displacements and three rotations components, which become two displacements and one rotation component in the 2D case here considered so that the displacement vector $\{u\}^T = \{u_1 \ u_2 \ \omega\}$ applies. In the present 2D linearized framework the strain displacement vector is represented as: $\{\varepsilon\}^T = \{\{\varepsilon_1\} \ \{\varepsilon_2\}\}$, where $\{\varepsilon_1\} = \{\varepsilon_{11} \ \varepsilon_{22} \ k_1 \ k_2\}$ and $\{\varepsilon_2\} = \{\varepsilon_{12} \ \varepsilon_{21}\}$ and where $\varepsilon_{11}, \varepsilon_{22}, \varepsilon_{12}, \varepsilon_{21}$ are the in-plane normal and shear strains and k_1, k_2 are the micropolar curvatures. Note that the strain components are not reciprocal, $\varepsilon_{12} \neq \varepsilon_{21}$. The kinematic compatibility relations can be written as: $\{\varepsilon_1\} = [D_1]\{u\}$ and $\{\varepsilon_2\} = [D_2]\{u\}$

$$[D_1] = \begin{bmatrix} \partial/\partial x_1 & 0 & 0 \\ 0 & \partial/\partial x_2 & 0 \\ 0 & 0 & \partial/\partial x_1 \\ 0 & 0 & \partial/\partial x_2 \end{bmatrix}, \quad [D_2] = \begin{bmatrix} \partial/\partial x_2 & 0 & 1 \\ 0 & \partial/\partial x_1 & -1 \end{bmatrix} \quad (1)$$

Note that in general the microrotation, ω , in the micropolar model is different from the local rigid rotation (macro-rotation), θ , defined as the skew-symmetric part of the gradient of displacement $\theta = \frac{1}{2}(\frac{\partial u_2}{\partial x_1} - \frac{\partial u_1}{\partial x_2})$ and the difference between the two rotations, $\theta - \omega$, defines the strain measure of the relative rotation that corresponds to the skew-symmetric part of the strain: $\theta = \frac{1}{2}(\frac{\partial u_2}{\partial x_1} - \frac{\partial u_1}{\partial x_2})$. When the relative rotation equals zero, $\theta = \omega$ and $\varepsilon_{12} = \varepsilon_{21} = \frac{1}{2}(\frac{\partial u_1}{\partial x_2} + \frac{\partial u_2}{\partial x_1})$, as in the classical continuum, the micropolar continuum becomes a continuum with constrained rotations (Masiani and Trovalusci, 1996; Sokolowski, 1972). In the following, we focus on $\theta - \omega$ as peculiar strain measure of the micropolarity of the model under study.

Analogously, the work-conjugated stress measures of the micropolar model are represented in the vector: $\{\sigma\}^T = \{\{\sigma_1\} \ \{\sigma_2\}\}$ with $\{\sigma_1\}^T = \{\sigma_{11} \ \sigma_{22} \ \mu_1 \ \mu_2\}$ and $\{\sigma_2\}^T = \{\sigma_{12} \ \sigma_{21}\}$, where σ_{ij} for $i, j = 1, 2$ represent the classical normal and shear stress components, and μ_1, μ_2 are the microcouples. The stress components are not reciprocal, $\sigma_{12} \neq \sigma_{21}$, and the couple stress components, μ_1, μ_2 , have to be introduced in order to satisfy the moment equilibrium of the micropolar body. From the virtual work principle without introducing the constitutive equations, described below, equilibrium equations in terms of stresses and microcouples can be carried out as $\delta U + \delta V = 0$, so that

$$\begin{aligned} \delta U &= \int_V \{\delta \varepsilon\}^T \{\sigma\} dV = \int_V \left(\{\delta \varepsilon_1\}^T \{\sigma_1\} + \{\delta \varepsilon_2\}^T \{\sigma_2\} \right) dV \\ &= \{\delta u\}^T h \int_A \left([D_1]^T \{\sigma_1\} + [D_2]^T \{\sigma_2\} \right) dA \end{aligned} \quad (2)$$

h being the thickness of the 2D domain which can be considered as unitary for plane strain case, and where the variation of potential of the external loads reads:

$$\delta V = - \int_A \{\delta u\}^T \{f\} dA - \int_S \{\delta u\}^T \{p\} dS \quad (3)$$

where $\{f\}$ and $\{p\}$ are the vectors of body forces and boundary tractions, respectively. Finally, balance domain equations are given by

$$[D_1]^T \{\sigma_1\} + [D_2]^T \{\sigma_2\} = \{f\} \quad (4)$$

and boundary tractions as:

$$\{p\} = \{\hat{p}\} \quad (5)$$

where $\{\hat{p}\}$ are stresses and microcouples applied at the boundary.

The micropolar constitutive equations take the form:

$$\begin{Bmatrix} \{\sigma_1\} \\ \{\sigma_2\} \end{Bmatrix} = \begin{bmatrix} \mathbb{C}_{11} & \mathbb{C}_{12} \\ \mathbb{C}_{21} & \mathbb{C}_{22} \end{bmatrix} \begin{Bmatrix} \{\varepsilon_1\} \\ \{\varepsilon_2\} \end{Bmatrix} \quad (6)$$

and

$$\begin{aligned} \mathbb{C}_{11} &= \begin{bmatrix} A_{1111} & A_{1122} & B_{111} & B_{112} \\ A_{1122} & A_{2222} & B_{221} & B_{222} \\ B_{111} & B_{221} & D_{11} & D_{12} \\ B_{112} & B_{222} & D_{12} & D_{22} \end{bmatrix}, & \mathbb{C}_{12} &= \begin{bmatrix} A_{1112} & A_{1121} \\ A_{2212} & A_{2221} \\ B_{121} & B_{211} \\ B_{122} & B_{212} \end{bmatrix} \\ \mathbb{C}_{21} &= \begin{bmatrix} A_{1112} & A_{2212} & B_{121} & B_{122} \\ A_{1121} & A_{2221} & B_{211} & B_{212} \end{bmatrix}, & \mathbb{C}_{22} &= \begin{bmatrix} A_{1212} & A_{1221} \\ A_{1221} & A_{2121} \end{bmatrix} \end{aligned} \quad (7)$$

Due to hyperelasticity the constitutive matrix is symmetrical: $\mathbb{C}_{12} = \mathbb{C}_{21}^T$. Note that the symbols A_{ijkl} , B_{ijk} , and D_{ij} (for $i, j, k, l = 1, 2$) in definitions (7) can be collected in the matrices \mathbb{A} , \mathbb{B} , and \mathbb{D} as in Fantuzzi et al. (2019) and Leonetti et al. (2019). The homogenization technique presented by Trovalusci and Masiani (1999) is used to identify the constitutive constants of Eq. (6) from a given representative volume element (RVE) of elastically interacting rigid block assemblies.

The virtual work principle allows us to write the variational statement of the equilibrium for the present micropolar body $\delta U + \delta V = 0$, where the variation of the strain energy in terms of kinematic parameters reads:

$$\begin{aligned} \delta U &= \int_{\mathcal{V}} \{\delta \varepsilon\}^T \{\sigma\} d\mathcal{V} \\ &= \int_{\mathcal{V}} \left(\{\delta \varepsilon_1\}^T \mathbb{C}_{11} \{\varepsilon_1\} + \{\delta \varepsilon_1\}^T \mathbb{C}_{12} \{\varepsilon_2\} + \{\delta \varepsilon_2\}^T \mathbb{C}_{21} \{\varepsilon_1\} + \{\delta \varepsilon_2\}^T \mathbb{C}_{22} \{\varepsilon_2\} \right) d\mathcal{V} \\ &= \{\delta u\}^T \left[h \int_{\mathcal{A}} \left(\{D_1\}^T \mathbb{C}_{11} \{D_1\} + \{D_1\}^T \mathbb{C}_{12} \{D_2\} + \{D_2\}^T \mathbb{C}_{21} \{D_1\} + \{D_2\}^T \mathbb{C}_{22} \{D_2\} \right) d\mathcal{A} \right] \{u\} \end{aligned} \quad (8)$$

In the following, the finite element approximation will be applied directly to the variational principle as that to Eqs. (3) and (8).

3. HEXAGONAL PATTERN

The irregular pattern of Fig. 1 has been taken from the studies by Scherphuis (2019) which is given by convex hexagon tilings of type 1 (P6). The correspondent Representative Volume Element (RVE) is given in Fig. 1 which shows the centroids of the tiles and outward unit normal vectors at the block interfaces used for computing the constitutive matrix according to the procedure presented by Trovalusci and Masiani (1999).

Given a list of input parameters: three angles $\alpha_1, \alpha_2, \alpha_3$, relative length, l_r , and a tile scale, s , the single hexagon, tile, can be defined. Using simple geometric formulas the RVE can be defined by translations and mirroring of tiles.

The single tile is defined by a parallelogram (skew rectangle) and two isosceles triangles with the base attached to the two shortest opposite sides of the parallelogram.

With reference to Fig. 1, the nodal coordinates of the single tile are given by: $A \equiv (0, 0)$, $B \equiv (l_1, t)$, $C \equiv (l_1 + l_5, t + l_2/2)$, $D \equiv (l_1, t + l_2)$, $E \equiv (0, l_2)$, $F \equiv (-l_4, l_2/2)$ where $l_2 = s \frac{l_r}{100}$, $l_1 = s - l_2$, $t = l_1 \tan \alpha_1$, $l_4 = \frac{l_2}{2} \tan \alpha_2$, $l_5 = \frac{l_2}{2} \tan \alpha_3$ and s is a scale parameter. Relations among tile side lengths a to f can be easily carried out using classical geometric relationships.

By changing the geometric parameters listed above, several patterns can be obtained as the ones depicted in Fig. 2 which are termed for future reference: regular, hourglass, and chiral, respectively. They have been obtained by setting

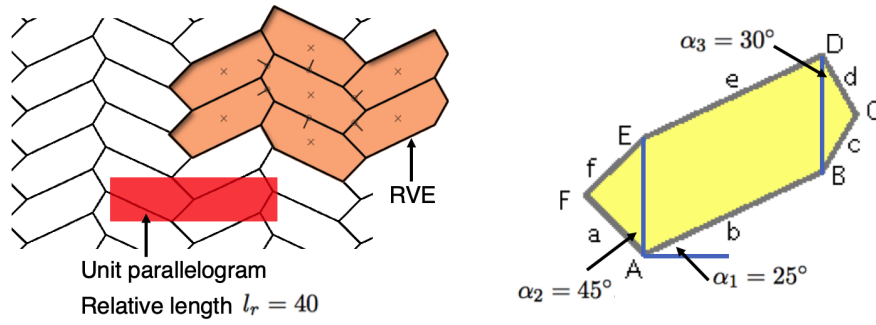


FIG. 1: Irregular hexagonal pattern and single tile with geometric parameters $\alpha_1 = 25^\circ$, $l_r = 40$, $\alpha_2 = 45^\circ$, $\alpha_3 = 30^\circ$

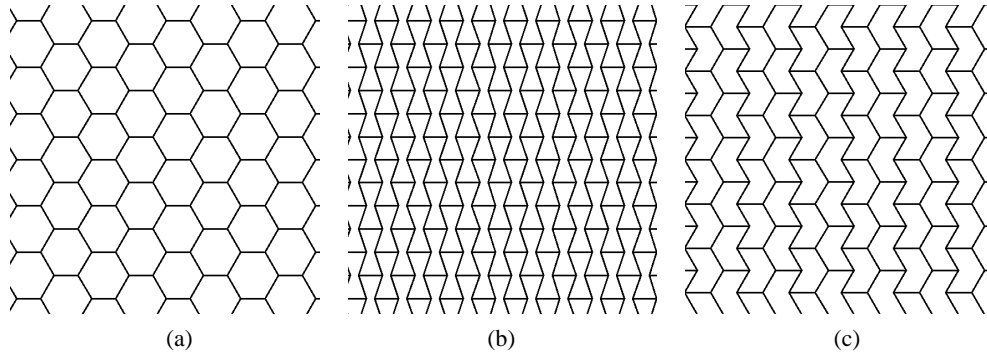


FIG. 2: Hexagonal patterns given by geometric parameters $\alpha_1 = 0^\circ$, $l_r = \frac{100}{1/\sqrt{3}+1}$: (a) regular $\alpha_2 = \alpha_3 = 30^\circ$, (b) hourglass $\alpha_2 = \alpha_3 = -20^\circ$, and (c) chiral $-\alpha_2 = \alpha_3 = 30^\circ$

a equilateral geometry (all the sides – a to f – have the same length) with $\alpha_1 = 0^\circ$, $l_r = \frac{100}{1/\sqrt{3}+1} \cong 63.3975$, and by varying α_2 and α_3 angles as:

1. Regular: $\alpha_2 = \alpha_3 = 30^\circ$
2. Hourglass: $\alpha_2 = \alpha_3 = -20^\circ$
3. Chiral: $-\alpha_2 = \alpha_3 = 30^\circ$

For the three scales considered the tiles have the following side lengths:

- $s = 1 \rightarrow l_1 = 0.3660$
- $s = 0.5 \rightarrow l_1 = 0.1830$
- $s = 0.25 \rightarrow l_1 = 0.0915$

so smaller scales lead to smaller tile sizes and vice versa.

4. FINITE ELEMENT IMPLEMENTATION

The present finite element framework is based on the previous studies by Fantuzzi et al. (2019) and Leonetti et al. (2019). However, the present implementation has been performed with an in-house MATLAB code as an extension of the classical 2D plane strain Cauchy continuum, as presented by Ferreira (2008).

As it is well-known the classical finite element method enforces an approximation through nodal kinematic parameters as $\{u\} = \mathbb{N}\{d^e\}$. In this work finite elements with four nodes (Q4) are considered, so that the vector of

nodal parameters reads $\{d^e\}^T = \{u_1^1 \dots u_1^4 \ u_2^1 \dots u_2^4 \ \omega^1 \dots \omega^4\}$, thus each finite element has 12 degrees of freedom (DOF). Linear shape functions are considered for the present implementation with reduced integration for the microrotation ω because unsymmetric strains ε_{12} and ε_{21} will not be given by the same order of quantities. The matrix of the shape functions (of size 3×12) takes the form

$$\mathbb{N} = \begin{bmatrix} \{N\} & \{0\} & \{0\} \\ \{0\} & \{N\} & \{0\} \\ \{0\} & \{0\} & \{N\} \end{bmatrix} \quad (9)$$

where $\{N\}$ is the vector of the Lagrangian linear shape functions. Some implementations consider different shape functions among displacements and microrotations (Fantuzzi et al., 2018; Leonetti et al., 2019) in order to avoid element locking due to shear strains that have derivative of the planar strains summed with microrotation. By inserting the finite element approximation $\{u\} = \mathbb{N}\{d^e\}$ in the strain energy definition (8) as:

$$\delta U = \{\delta d^e\}^T h \int_{\mathcal{A}} \left(\{B_1\}^T \mathbb{C}_{11} \{B_1\} + \{B_1\}^T \mathbb{C}_{12} \{B_2\} + \{B_2\}^T \mathbb{C}_{21} \{B_1\} + \{B_2\}^T \mathbb{C}_{22} \{B_2\} \right) d\mathcal{A} \{d^e\} \quad (10)$$

where $\{B_1\} = \{D_2\}\mathbb{N}$ and $\{B_2\} = \{D_2\}\mathbb{N}$, thus the element stiffness matrix is

$$[K^e] = [K_1^e] + [K_2^e] \quad (11)$$

where

$$[K_1^e] = h \int_{\mathcal{A}} \left(\{B_1\}^T \mathbb{C}_{11} \{B_1\} + \{B_1\}^T \mathbb{C}_{12} \{B_2\} + \{B_2\}^T \mathbb{C}_{21} \{B_1\} \right) d\mathcal{A} \quad (12)$$

$$[K_2^e] = h \int_{\mathcal{A}} \left(\{B_2\}^T \mathbb{C}_{22} \{B_2\} \right) d\mathcal{A} \quad (13)$$

Full integration (2×2 Gauss integration) is performed on $[K_1^e]$, whereas shear strain terms $[K_2^e]$ are integrated using single-point reduced integration.

Finally, potential energy (3) becomes:

$$\delta V = -\delta\{d^e\}^T h \int_{\mathcal{A}} \mathbb{N}^T \{f\} d\mathcal{V} - \delta\{d^e\}^T \int_{\mathcal{S}} \mathbb{N}^T \{p\} d\mathcal{S} = -\delta\{d^e\}^T (\{F^e\} + \{P^e\}) \quad (14)$$

where $\{F^e\}$ and $\{P^e\}$ are volume and surface force vectors, respectively. In the present work, only surface tractions are applied so that $\{F^e\} = \{0\}$.

4.1 Post-Computation

Since the present formulation is based on displacements, in order to carry out strain and stress values at discretization nodes post-computation must be performed. It is well-established that derived quantities should be post-computed at integration points (Reddy, 2004, 2017). For Q4 elements the integration points used are a 2×2 Gauss–Legendre grid.

Strain and stresses are recovered from the kinematic compatibility and constitutive equations, respectively. The relative rotation, $\theta - \omega$, is used, as in previous papers (Fantuzzi et al., 2018, 2019; Leonetti et al., 2019; Trovalusci and Masiani, 1999), for underlining the micropolar effects with respect to the classical continuum. Relative relation

$$\theta - \omega = \left\{ -\frac{1}{2} \frac{\partial}{\partial x_2} \quad \frac{1}{2} \frac{\partial}{\partial x_1} \quad -1 \right\} \mathbb{N} \{d^e\} \quad (15)$$

However, field variables are more commonly defined at grid nodes. Thus, extrapolation of each field value is carried out for Q4 elements using the following formula:

$$\begin{bmatrix} w_1 \\ w_2 \\ w_3 \\ w_4 \end{bmatrix} = \begin{bmatrix} 1 + 0.5\sqrt{3} & -0.5 & 1 - 0.5\sqrt{3} & -0.5 \\ -0.5 & 1 + 0.5\sqrt{3} & -0.5 & 1 - 0.5\sqrt{3} \\ 1 - 0.5\sqrt{3} & -0.5 & 1 + 0.5\sqrt{3} & -0.5 \\ -0.5 & 1 - 0.5\sqrt{3} & -0.5 & 1 + 0.5\sqrt{3} \end{bmatrix} \begin{bmatrix} \hat{w}_1 \\ \hat{w}_2 \\ \hat{w}_3 \\ \hat{w}_4 \end{bmatrix} \quad (16)$$

where \hat{w}_i for $i = 1, \dots, 4$ are the extrapolated nodal values whereas w_i for $i = 1, \dots, 4$ are the correspondent internal field values.

Finally, inter-element averaging is applied with equal weights in order to have single values at each nodal point. This final procedure allows us to have an array of values one for each mesh grid point without intersections.

5. NUMERICAL RESULTS

A square panel of side $L = 4$ is considered subjected to a top pressure on a limited area $a = L/4$ with a resulting equivalent concentrated force of $P = 10^3$ pointing downward. The panel is clamped at the bottom. A regular squared FE mesh of 16×32 elements (by taking advantage of problem symmetry) is considered and depicted in Fig. 3.

In this section the numerical results for the three cited geometries are presented. In particular, the contour plots of displacements, u_1 (horizontal), and u_2 (vertical), stresses, σ_{11} (horizontal), σ_{22} (vertical), and relative rotation $\theta - \omega$ are shown for each geometry.

The homogenization procedure follows the approach described by Trovalusci and Masiani (1999), where the adopted spring stiffness at the elastic joint interfaces is

$$K_T = \begin{bmatrix} 785 & 0 \\ 0 & 780 \end{bmatrix}, \quad K_R = 0 \quad (17)$$

where K_T and K_R are the stiffnesses of translational and rotational springs. Energetic equivalence is used to carry out rotational stiffnesses as:

$$k_n = K_{T(1,1)} \frac{d}{2}, \quad k_r = k_n \frac{d^2}{2} = K_{T(1,1)} \frac{d^3}{4} \quad (18)$$

where d is the current interface length between two rigid particles for which the interactive stiffness is computed.

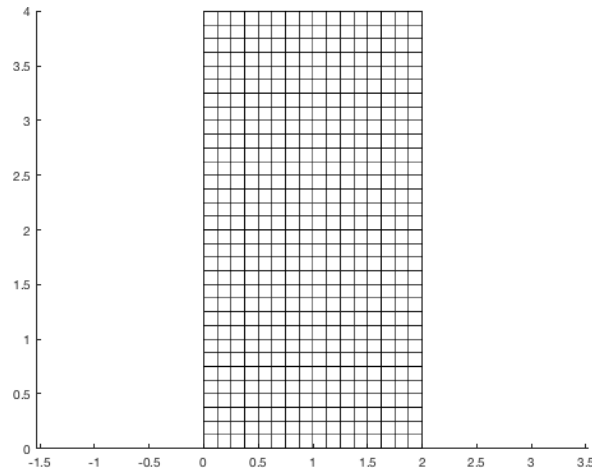


FIG. 3: Current mesh used 16×32 Q4 elements

For all three different scales, stiffness data (K_T and K_R , and consequently k_n and k_r) remain unchanged. The ratios between tile length and panel width l_1/L are 10.93, 21.86, 43.72 by decreasing scale, respectively. The constitutive matrices are presented below in compact and extended matrix form:

$$\mathbb{C} = \begin{bmatrix} \mathbb{A} & \mathbb{B} \\ \mathbb{B}^T & \mathbb{D} \end{bmatrix} = \begin{bmatrix} A_{1111} & A_{1122} & A_{1112} & A_{1121} & B_{111} & B_{112} \\ & A_{2222} & A_{2212} & A_{2221} & B_{221} & B_{222} \\ & & A_{1212} & A_{1221} & B_{121} & B_{122} \\ & & & A_{2121} & B_{211} & B_{212} \\ & & & & D_{11} & D_{12} \\ \text{sym} & & & & & D_{22} \end{bmatrix} \quad (19)$$

5.1 Orthotetragonal Hexagons

The aforementioned regular hexagons can be carried out from P6 geometry Scherphuis (2019) by setting: $l_r = 63.3975$, $\alpha_1 = 0^\circ$, $\alpha_2 = \alpha_3 = 30^\circ$. The results for the three scales $s = 1, 0.5, 0.25$ are depicted in Fig. 4, where tile centers and link orientations are shown for calculation purposes (Trovalusci and Masiani, 1999).

The correspondent constitutive matrices appear to be orthotetragonal (symmetric with respect to a 90° rotation) as:

$$\mathbb{C}_{\text{ortho}}^{(s=1)} = \begin{bmatrix} 496.8776 & 0.7925 & 0 & 0 & 0 & 0 \\ 0.7925 & 496.8776 & 0 & 0 & 0 & 0 \\ 0 & 0 & 495.2927 & 0.7925 & 0 & 0 \\ 0 & 0 & 0.7925 & 495.2927 & 0 & 0 \\ 0 & 0 & 0 & 0 & 33.3376 & 0 \\ 0 & 0 & 0 & 0 & 0 & 33.3376 \end{bmatrix} \quad (20)$$

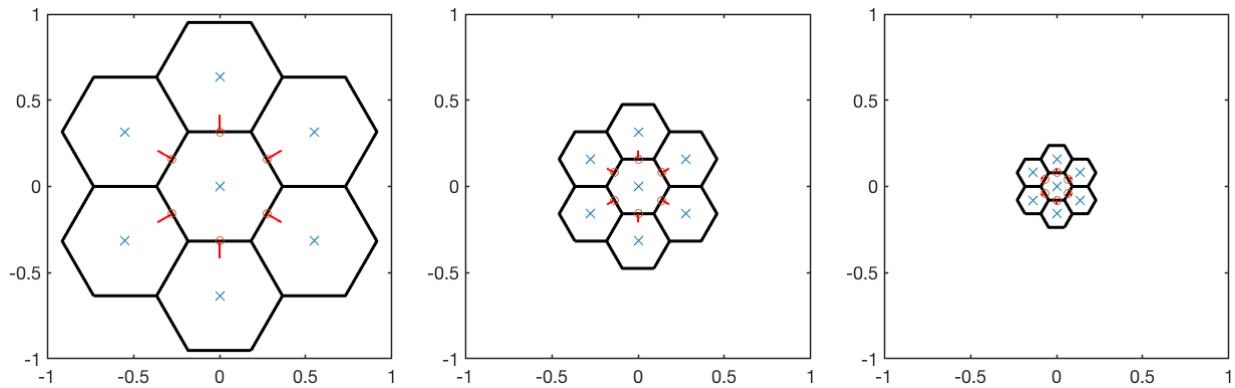


FIG. 4: Regular hexagonal pattern RVE with geometric parameters $\alpha_1 = 0^\circ$, $l_r = \frac{100}{1/\sqrt{3}+1}$, $\alpha_2 = \alpha_3 = 30^\circ$ at different scale $s = 1, 0.5, 0.25$ from left to right, respectively

$$\mathbb{C}_{\text{ortho}}^{(s=0.5)} = \begin{bmatrix} 248.4388 & 0.3962 & 0 & 0 & 0 & 0 \\ 0.3962 & 248.4388 & 0 & 0 & 0 & 0 \\ 0 & 0 & 247.6463 & 0.3962 & 0 & 0 \\ 0 & 0 & 0.3962 & 247.6463 & 0 & 0 \\ 0 & 0 & 0 & 0 & 4.1672 & 0 \\ 0 & 0 & 0 & 0 & 0 & 4.1672 \end{bmatrix} \quad (21)$$

$$\mathbb{C}_{\text{ortho}}^{(s=0.25)} = \begin{bmatrix} 124.2194 & 0.1981 & 0 & 0 & 0 & 0 \\ 0.1981 & 124.2194 & 0 & 0 & 0 & 0 \\ 0 & 0 & 123.8232 & 0.1981 & 0 & 0 \\ 0 & 0 & 0.1981 & 123.8232 & 0 & 0 \\ 0 & 0 & 0 & 0 & 0.5209 & 0 \\ 0 & 0 & 0 & 0 & 0 & 0.5209 \end{bmatrix} \quad (22)$$

In such orthotetragonal assemblies $A_{1111} = A_{2222}$ and $A_{1212} = A_{2121}$ as well as $D_{11} = D_{22}$; moreover, there is no coupling between normal and shear stresses and at the same time between microcouples ($D_{12} = 0$) and $\mathbb{B} = 0$ and thus no elastic coefficients relating stresses and strains and coefficients relating microcouples and curvatures are expected. A very small Poisson effect is also shown. The ratios between elastic coefficients relating stresses and strains between different scales is 2, whereas between coefficients relating microcouples and curvatures is 8 [$\mathbb{A}^{(s=1)} = 2\mathbb{A}^{(s=0.5)} = 4\mathbb{A}^{(s=0.25)}$ and $\mathbb{D}^{(s=1)} = 8\mathbb{D}^{(s=0.5)} = 64\mathbb{D}^{(s=0.25)}$].

The numerical results obtained are shown in Figs. 5–9 for the three mentioned scales. We can observe that in such a case of localized load the micropolar model is able to better distribute the load depending on the material internal length related to the tile size. In particular, the vertical displacement, u_2 , tends to concentrate on the central part of the wall for smaller scales with more remarkable values with respect to larger scales (Fig. 6). Due to vertical pressure the body also tends to move horizontally, u_1 . Figure 5 displays such effect which is more evident for smaller scales.

Horizontal pressures, σ_{11} , (Fig. 7) are almost negligible for larger scales. For small scales these stresses concentrate in the area below the applied load. The same effect is more clear for the vertical stress, σ_{22} , where a distinct flux of stress is clearly visible for smaller scales (Fig. 8).

Finally, the relative rotation, $\theta - \omega$, plot (Fig. 9) shows a very small micropolar effect as expected since orthotetragonal materials are known to be very close to Cauchy continua, as already discussed in Trovalusci and Masiani (1999).

5.2 Hourglass Hexagons

By keeping the symmetry of the single tile and equilateral tile segments, the inner angles $\alpha_2 = \alpha_3 = -20^\circ$ are set to a negative value. Graphical representation of the three cells with different scale is given in Fig. 10.

This leads to an auxetic behavior of the homogenized material, with negative Poisson coefficient ($A_{1122} < 0$), for all three cases considered as it is shown by the constitutive matrices given below:

$$\mathbb{C}_{\text{hour}}^{(s=1)} = \begin{bmatrix} 209.2 & -0.5 & 0 & 0 & 0 & 0 \\ -0.5 & 1059.7 & 0 & 0 & 0 & 0 \\ 0 & 0 & 1056.8 & -0.5 & 0 & 0 \\ 0 & 0 & -0.5 & 208.2 & 0 & 0 \\ 0 & 0 & 0 & 0 & 11.9 & 0 \\ 0 & 0 & 0 & 0 & 0 & 67.7 \end{bmatrix} \quad (23)$$

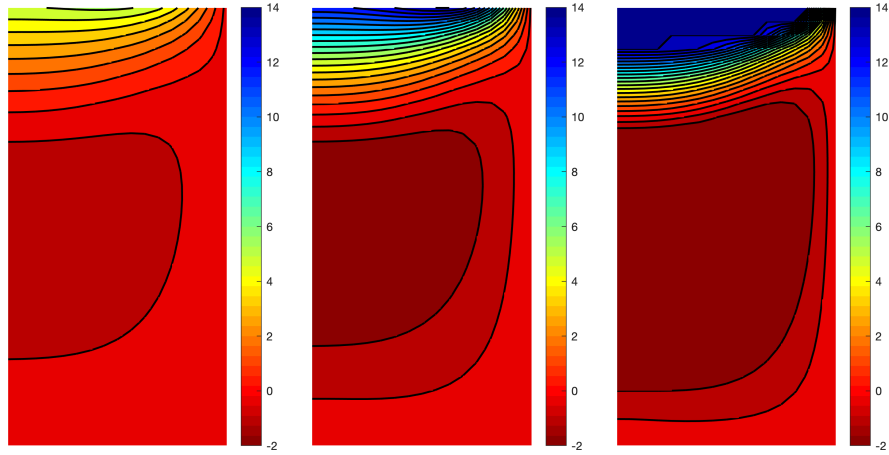


FIG. 5: Q4 formulation. Horizontal displacement u_1 for regular hexagonal patterns with parameters $\alpha_1 = 0^\circ$, $l_r = \frac{100}{1/\sqrt{3}+1}$, $\alpha_2 = \alpha_3 = 30^\circ$ and scales $s = 1, 0.5, 0.25$ from left to right, respectively.

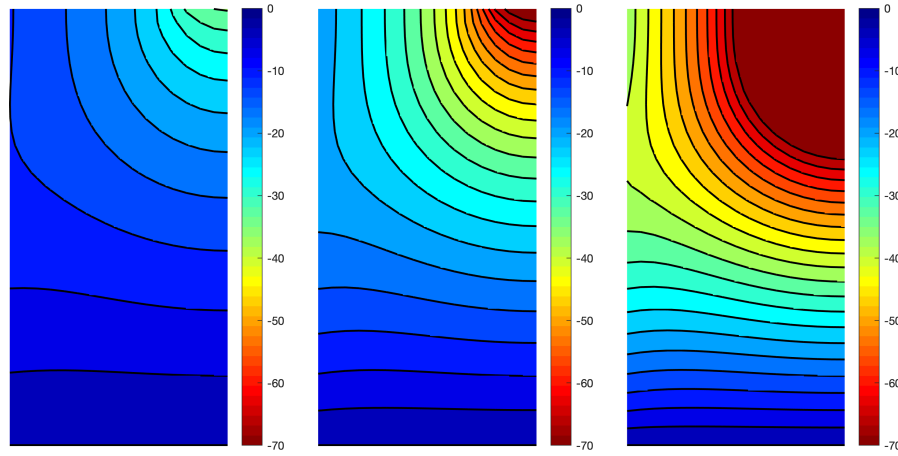


FIG. 6: Q4 formulation. Vertical displacement u_2 for regular hexagonal patterns with parameters $\alpha_1 = 0^\circ$, $l_r = \frac{100}{1/\sqrt{3}+1}$, $\alpha_2 = \alpha_3 = 30^\circ$ and scales $s = 1, 0.5, 0.25$ from left to right, respectively.

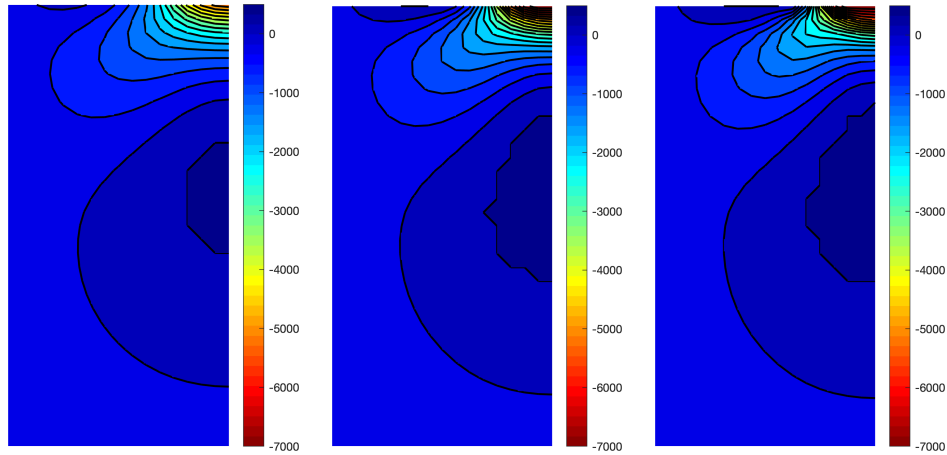


FIG. 7: Q4 formulation. Horizontal stress σ_{11} for regular hexagonal patterns with parameters $\alpha_1 = 0^\circ$, $l_r = \frac{100}{1/\sqrt{3}+1}$, $\alpha_2 = \alpha_3 = 30^\circ$ and scales $s = 1, 0.5, 0.25$ from left to right, respectively.

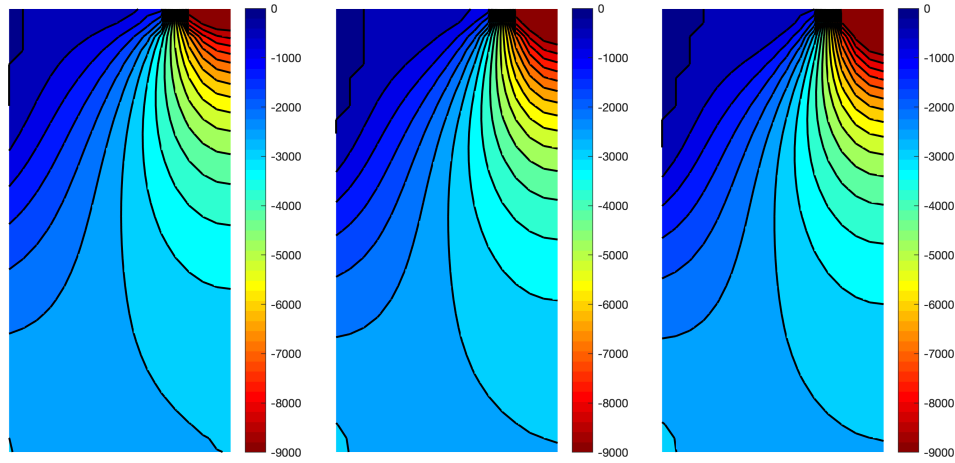


FIG. 8: Q4 formulation. Vertical stress σ_{22} for regular hexagonal patterns with parameters $\alpha_1 = 0^\circ$, $l_r = \frac{100}{1/\sqrt{3}+1}$, $\alpha_2 = \alpha_3 = 30^\circ$ and scales $s = 1, 0.5, 0.25$ from left to right, respectively.

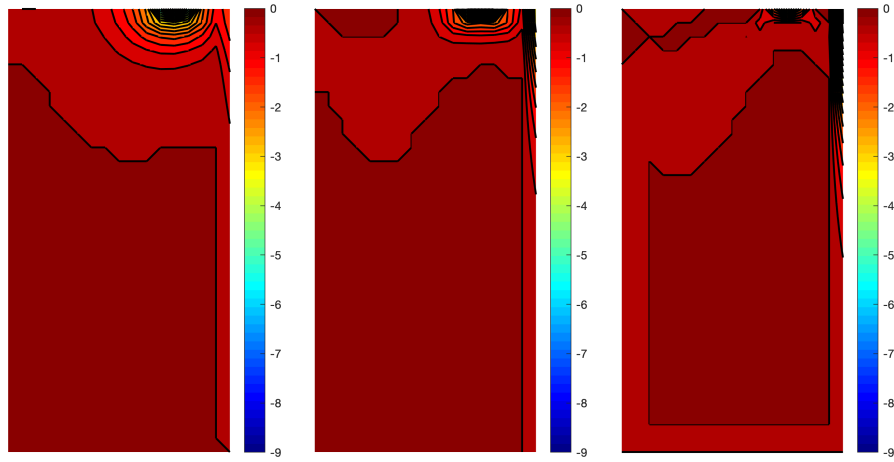


FIG. 9: Q4 formulation. Relative rotation $\theta - \omega$ for regular hexagonal patterns with parameters $\alpha_1 = 0^\circ$, $l_r = \frac{100}{1/\sqrt{3}+1}$, $\alpha_2 = \alpha_3 = 30^\circ$ and scales $s = 1, 0.5, 0.25$ from left to right, respectively.

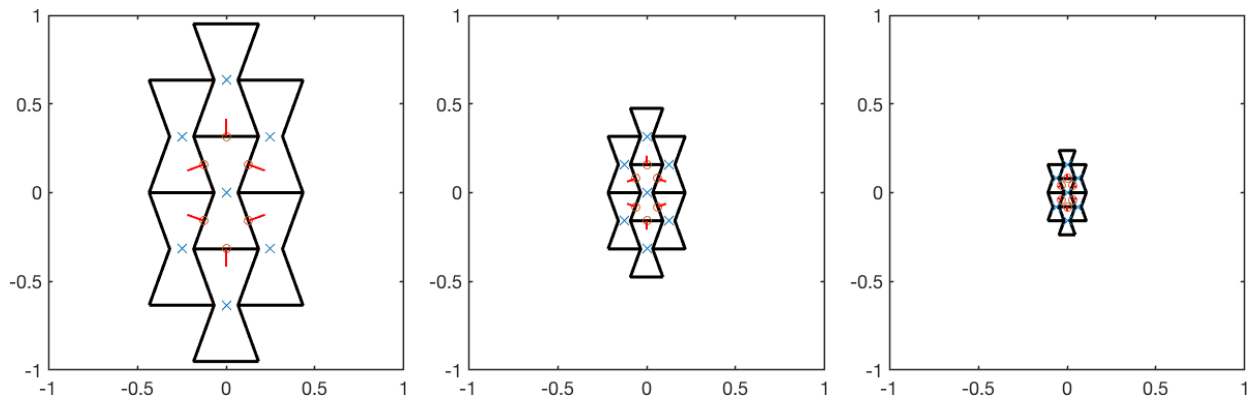


FIG. 10: Hourglass hexagonal pattern RVE with geometric parameters $\alpha_1 = 0^\circ$, $l_r = \frac{100}{1/\sqrt{3}+1}$, $\alpha_2 = \alpha_3 = -20^\circ$ at different scale $s = 1, 0.5, 0.25$ from left to right, respectively

$$\mathbb{C}_{\text{hour}}^{(s=0.5)} = \begin{bmatrix} 104.6165 & -0.2710 & 0 & 0 & 0 & 0 \\ -0.2710 & 529.8742 & 0 & 0 & 0 & 0 \\ 0 & 0 & 528.3768 & -0.2710 & 0 & 0 \\ 0 & 0 & -0.2710 & 104.1057 & 0 & 0 \\ 0 & 0 & 0 & 0 & 1.4892 & 0 \\ 0 & 0 & 0 & 0 & 0 & 8.4671 \end{bmatrix} \quad (24)$$

$$\mathbb{C}_{\text{hour}}^{(s=0.25)} = \begin{bmatrix} 52.3083 & -0.1355 & 0 & 0 & 0 & 0 \\ -0.1355 & 264.9371 & 0 & 0 & 0 & 0 \\ 0 & 0 & 264.1884 & -0.1355 & 0 & 0 \\ 0 & 0 & -0.1355 & 52.0529 & 0 & 0 \\ 0 & 0 & 0 & 0 & 0.1861 & 0 \\ 0 & 0 & 0 & 0 & 0 & 1.0584 \end{bmatrix} \quad (25)$$

The ratio between elastic coefficients relating stresses and strains and coefficients relating microcouples and curvatures results as in the previous case [$\mathbb{A}^{(s=1)} = 2\mathbb{A}^{(s=0.5)} = 4\mathbb{A}^{(s=0.25)}$; $\mathbb{D}^{(s=1)} = 8\mathbb{D}^{(s=0.5)} = 64\mathbb{D}^{(s=0.25)}$]. In addition, $A_{1111} \cong A_{2121}$, $A_{2222} \cong A_{1212}$ where the former are circa 5 times the latter and $5.69D_{11} \cong D_{22}$.

Numerical results are given in Figs. 11–15. The auxetic effect can be clearly seen in the horizontal displacements u_1 plot (Fig. 11) where the particles move on the right—towards the panel central area—this effect is quite small for larger particles and increases rapidly for smaller scales.

Vertical displacements, u_2 , (Fig. 12), stresses, σ_{11} , σ_{22} (Figs. 13 and 14), have comparable behavior with respect to the correspondent orthotetragonal cases but they have smaller intensity. It is remarked that the vertical stress is better diffused within the panel more in the case of larger size, in fact remarkable stress values are shown in Fig. 14 which are higher than the ones of the correspondent orthotetragonal case 8.

Relative rotation, $\theta - \omega$ (Fig. 15), shows a clear micropolar effect which increases when the scale s is decreased; this means that such a micropolar effect is stronger for smaller particles.

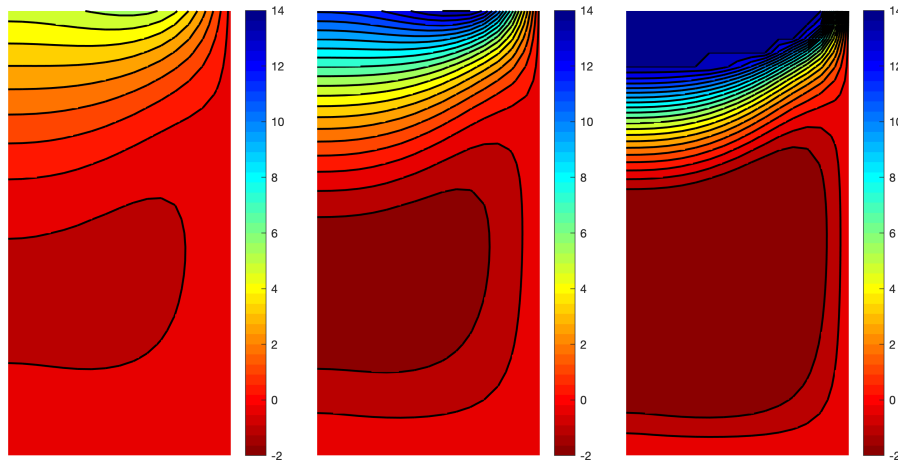


FIG. 11: Q4 formulation. Horizontal displacement u_1 for hourglass hexagonal patterns with parameters $\alpha_1 = 0^\circ$, $l_r = \frac{100}{1/\sqrt{3}+1}$, $\alpha_2 = \alpha_3 = -20^\circ$ and scales $s = 1, 0.5, 0.25$ from left to right, respectively.

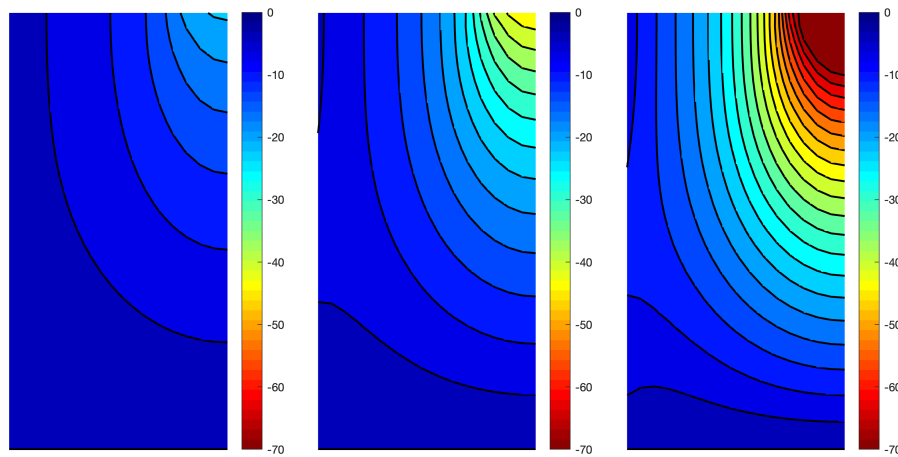


FIG. 12: Q4 formulation. Vertical displacement u_2 for hourglass hexagonal patterns with parameters $\alpha_1 = 0^\circ$, $l_r = \frac{100}{1/\sqrt{3}+1}$, $\alpha_2 = \alpha_3 = -20^\circ$ and scales $s = 1, 0.5, 0.25$ from left to right, respectively.

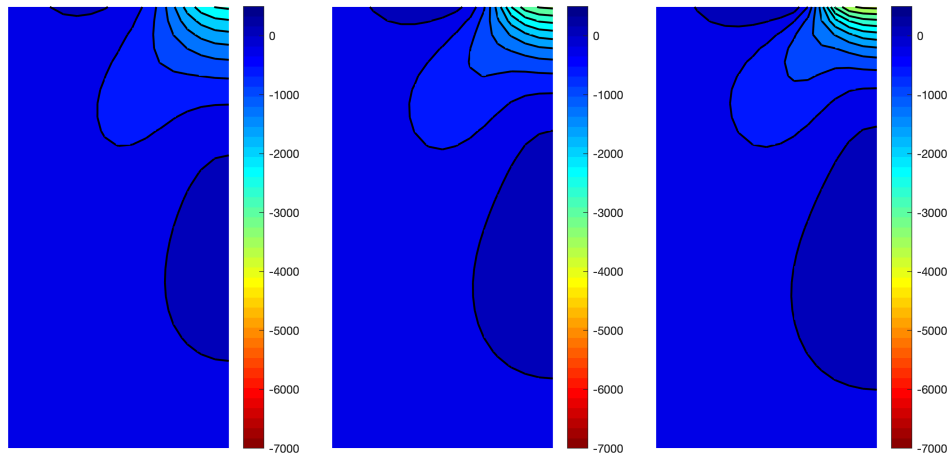


FIG. 13: Q4 formulation. Vertical stress σ_{11} for hourglass hexagonal patterns with parameters $\alpha_1 = 0^\circ$, $l_r = \frac{100}{1/\sqrt{3}+1}$, $\alpha_2 = \alpha_3 = -20^\circ$ and scales $s = 1, 0.5, 0.25$ from left to right, respectively.

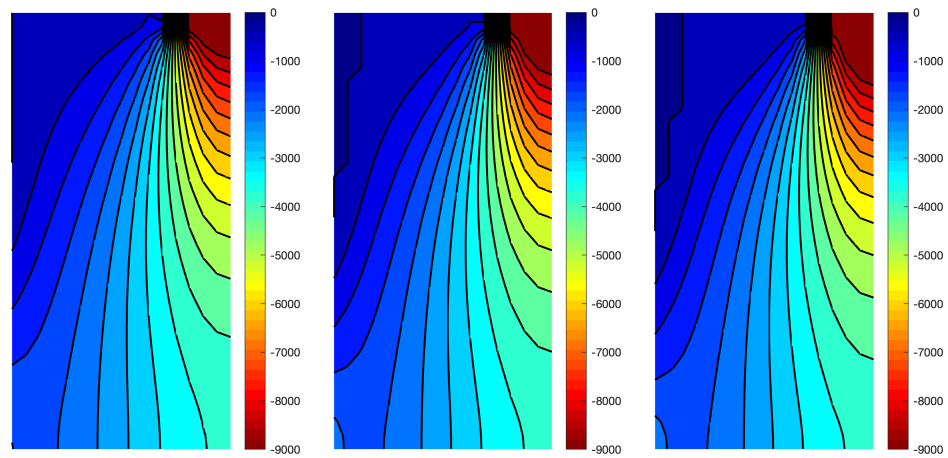


FIG. 14: Q4 formulation. Vertical stress σ_{22} for hourglass hexagonal patterns with parameters $\alpha_1 = 0^\circ$, $l_r = \frac{100}{1/\sqrt{3}+1}$, $\alpha_2 = \alpha_3 = -20^\circ$ and scales $s = 1, 0.5, 0.25$ from left to right, respectively.

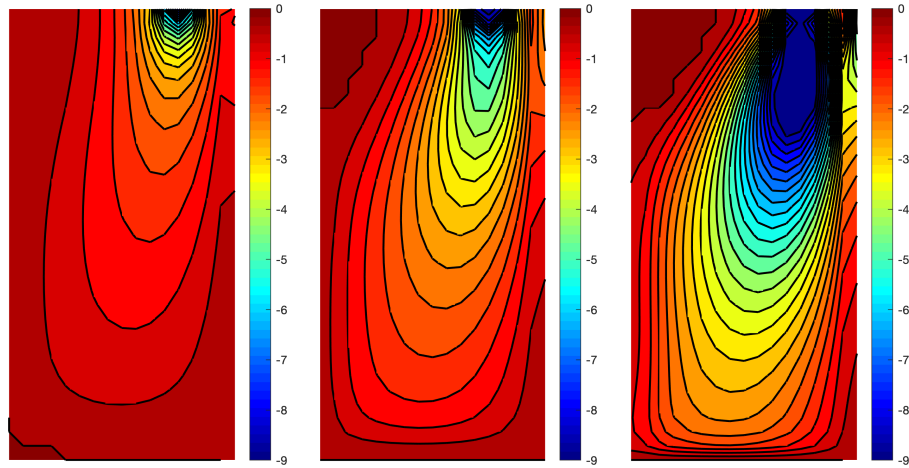


FIG. 15: Q4 formulation. Relative rotation $\theta - \omega$ for hourglass hexagonal patterns with parameters $\alpha_1 = 0^\circ$, $l_r = \frac{100}{1/\sqrt{3}+1}$, $\alpha_2 = \alpha_3 = -20^\circ$ and scales $s = 1, 0.5, 0.25$ from left to right, respectively.

5.3 Chiral Hexagons

The present geometry is obtained considering equilateral hexagons with inner angles $-\alpha_2 = \alpha_3 = 30^\circ$. Graphical representation of the three cells with different scale is given in Fig. 16.

The present geometrical selection leads to the following homogenized materials for the three given scales:

$$\mathbb{C}_{\text{chi}}^{(s=1)} = \begin{bmatrix} 331.2517 & 0 & 0 & 0 & 0 & 0 \\ 0 & 745.3164 & 0 & 0 & 0 & 45.5400 \\ 0 & 0 & 742.9390 & 0 & 0 & 0 \\ 0 & 0 & 0 & 330.1951 & 0 & 0 \\ 0 & 0 & 0 & 0 & 22.2250 & 0 \\ 0 & 45.5400 & 0 & 0 & 0 & 50.0064 \end{bmatrix} \quad (26)$$

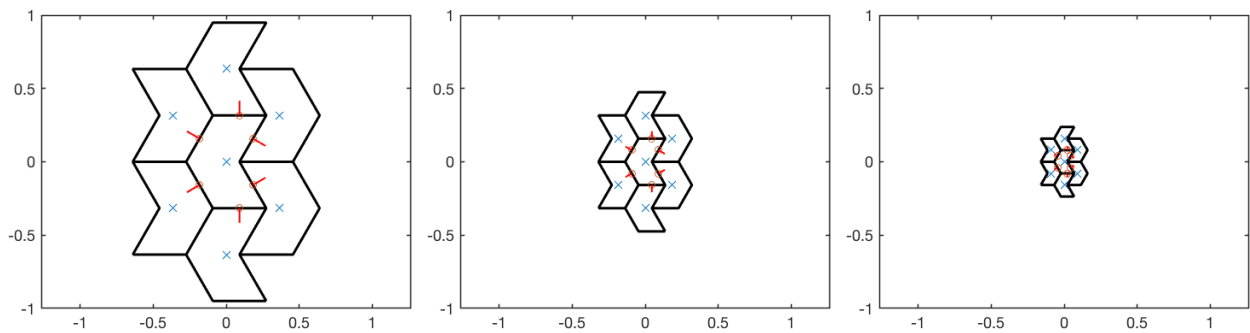


FIG. 16: Chiral hexagonal pattern RVE with geometric parameters $\alpha_1 = 0^\circ$, $l_r = \frac{100}{1/\sqrt{3}+1}$, $-\alpha_2 = \alpha_3 = 30^\circ$ at different scale $s = 1, 0.5, 0.25$ from left to right, respectively

$$\mathbb{C}_{\text{chi}}^{(s=0.5)} = \begin{bmatrix} 165.6259 & 0 & 0 & 0 & 0 & 0 \\ 0 & 372.6582 & 0 & 0 & 0 & 11.3850 \\ 0 & 0 & 371.4695 & 0 & 0 & 0 \\ 0 & 0 & 0 & 165.0976 & 0 & 0 \\ 0 & 0 & 0 & 0 & 2.7781 & 0 \\ 0 & 11.3850 & 0 & 0 & 0 & 6.2508 \end{bmatrix} \quad (27)$$

$$\mathbb{C}_{\text{chi}}^{(s=0.25)} = \begin{bmatrix} 82.8129 & 0 & 0 & 0 & 0 & 0 \\ 0 & 186.3291 & 0 & 0 & 0 & 2.8462 \\ 0 & 0 & 185.7347 & 0 & 0 & 0 \\ 0 & 0 & 0 & 82.5488 & 0 & 0 \\ 0 & 0 & 0 & 0 & 0.3473 & 0 \\ 0 & 2.8462 & 0 & 0 & 0 & 0.7813 \end{bmatrix} \quad (28)$$

Note that in this case a coupling between elastic coefficients relating stresses and strains and coefficients relating microcouples and curvatures occurs, implying coupling between normal stress σ_{22} and curvature k_2 and microcouple μ_2 and normal strain ε_2 . No other coupling takes place (also no Poisson effect is observed). Such behavior is due to the selection of equal and opposite angles $-\alpha_2 = \alpha_3 = 30^\circ$ which break material symmetry and neutralize lateral contraction/expansion. The ratio between coefficients relating stresses and strains and coefficients relating microcouples and curvatures is the same as in the previous microstructures [$\mathbb{A}^{(s=1)} = 2\mathbb{A}^{(s=0.5)} = 4\mathbb{A}^{(s=0.25)}$ and $\mathbb{D}^{(s=1)} = 8\mathbb{D}^{(s=0.5)} = 64\mathbb{D}^{(s=0.25)}$]. In addition, since $\mathbb{B} \neq 0$, $\mathbb{B}^{(s=1)} = 4\mathbb{B}^{(s=0.5)} = 16\mathbb{B}^{(s=0.25)}$. Similarly to the auxetic configuration, $A_{1111} \cong A_{2121}$, $A_{2222} \cong A_{1212}$, where the former are circa 2.25 times the latter and $2.27D_{11} \cong D_{22}$.

The numerical results are given in Figs. 17–21.

Since no Poisson effect is given in the constitutive equations negligible horizontal displacement u_1 (Fig. 17) and stress σ_{11} (Fig. 19) are observed. Vertical displacement u_2 (Fig. 18) and stress σ_{22} (Fig. 20) have a similar trend with respect to the other cases but closer to the auxetic one. The coupling in the present microstructure with $B_{222} \neq 0$

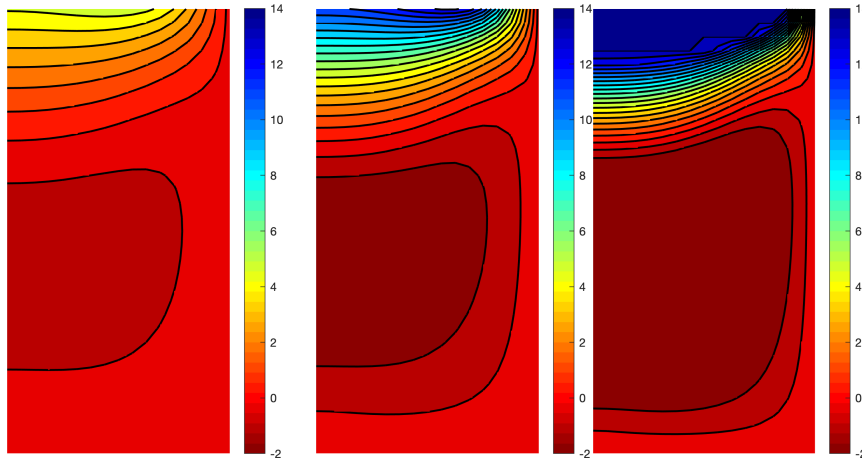


FIG. 17: Q4 formulation. Horizontal displacement u_1 for chiral hexagonal patterns with parameters $\alpha_1 = 0^\circ$, $l_r = \frac{100}{1/\sqrt{3}+1}$, $-\alpha_2 = \alpha_3 = 30^\circ$ and scales $s = 1, 0.5, 0.25$ from left to right, respectively.

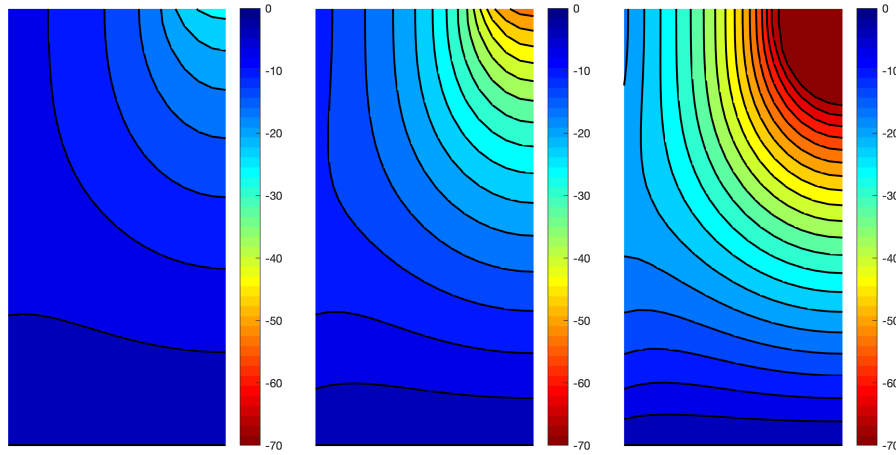


FIG. 18: Q4 formulation. Vertical displacement u_2 for chiral hexagonal patterns with parameters $\alpha_1 = 0^\circ$, $l_r = \frac{100}{1/\sqrt{3}+1}$, $-\alpha_2 = \alpha_3 = 30^\circ$ and scales $s = 1, 0.5, 0.25$ from left to right, respectively.

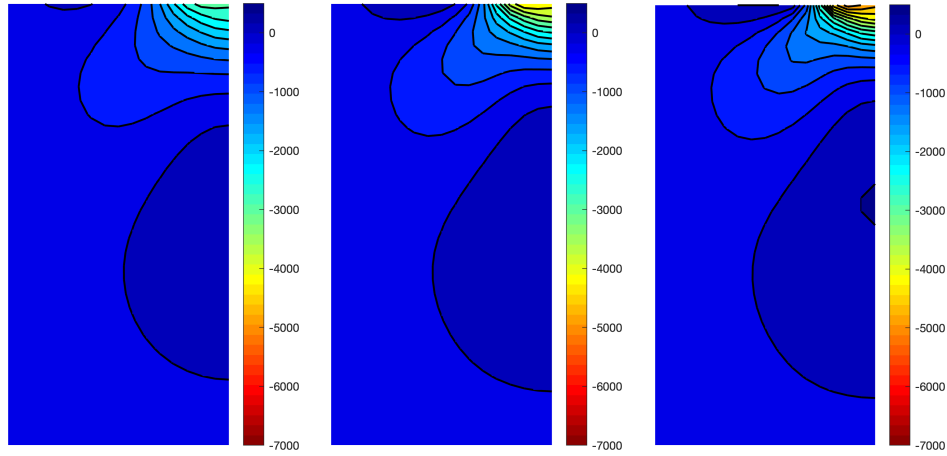


FIG. 19: Q4 formulation. Vertical stress σ_{11} for chiral hexagonal patterns with parameters $\alpha_1 = 0^\circ$, $l_r = \frac{100}{1/\sqrt{3}+1}$, $-\alpha_2 = \alpha_3 = 30^\circ$ and scales $s = 1, 0.5, 0.25$ from left to right, respectively.

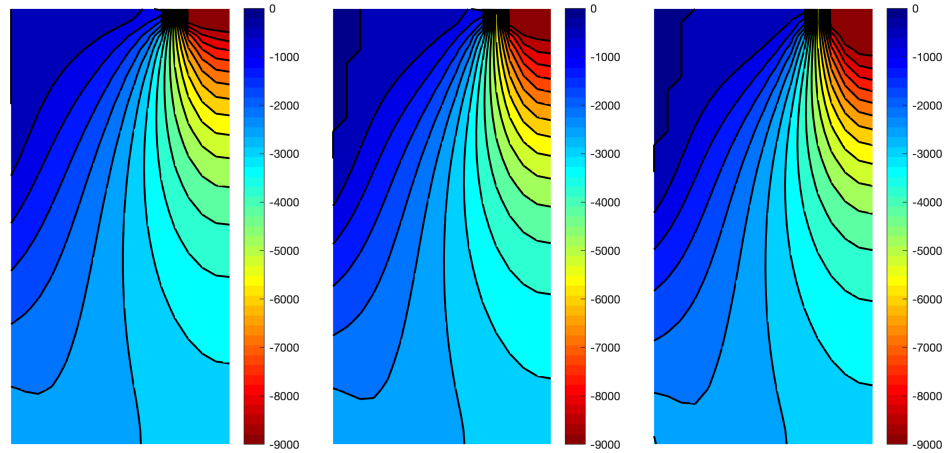


FIG. 20: Q4 formulation. Vertical stress σ_{22} for chiral hexagonal patterns with parameters $\alpha_1 = 0^\circ$, $l_r = \frac{100}{1/\sqrt{3}+1}$, $-\alpha_2 = \alpha_3 = 30^\circ$ and scales $s = 1, 0.5, 0.25$ from left to right, respectively.

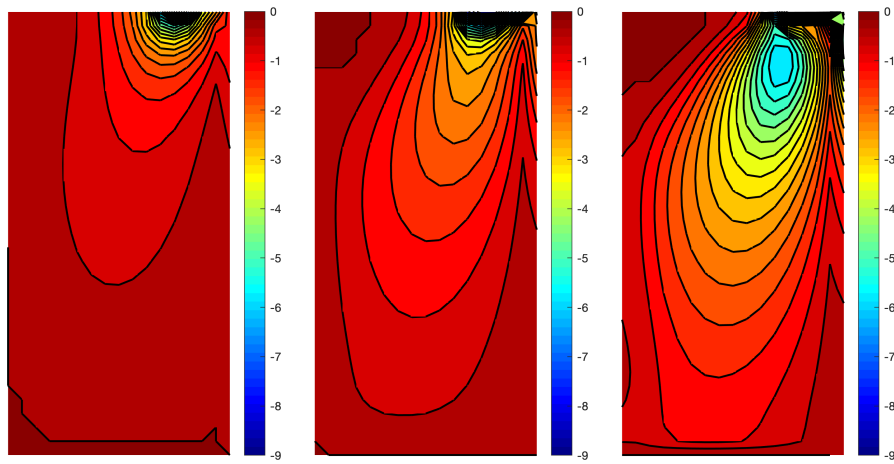


FIG. 21: Q4 formulation. Relative rotation $\theta - \omega$ for chiral hexagonal patterns with parameters $\alpha_1 = 0^\circ$, $l_r = \frac{100}{1/\sqrt{3}+1}$, $-\alpha_2 = \alpha_3 = 30^\circ$ and scales $s = 1, 0.5, 0.25$ from left to right, respectively.

gives a lower relative rotation effect than the one in the auxetic material but its variation is not uniform close to the symmetry axis, because the vertical pressure σ_{22} is coupled with the vertical curvature k_2 . This effect can be clearly observed for any scale s in Fig. 21.

6. CONCLUSIONS

The present work investigates the static behavior of materials with three types of hexagonal microstructures described as equivalent micropolar media. Such microstructures are typical of polycrystals with thin interfaces such as alumina (Al_2O_3), zirconia (ZrO_2), zinc oxide (ZnO) or tungsten-carbide (WC) just to cite a few. The three selected patterns provide orthotetragonal, auxetic, and chiral material symmetries and each one showed some peculiarities and some interesting outcomes related to the micropolar behavior. Assemblies of regular hexagons have an orthotetragonal behavior and it has been shown that their homogenized behavior is close to the behavior of classical elastic bodies (Masiani and Trovalusci, 1996; Trovalusci and Masiani, 2005). On the contrary, the other configurations showed strong nonlocal effects, related to the internal material size, which brought a larger stress diffusion within the body and reduced displacements. All these aspects could be underlined mostly because a micropolar continuum has extra rotational degrees of freedom with respect to classical continuum. If the coupling effect among classical and micropolar quantities wanted to be observed elastic interfaces among particles have to be as less symmetric as possible. Other geometries and interfaces configurations will be considered in future works in order to better understand the prediction of micropolar effects in microstructured materials.

ACKNOWLEDGMENTS

This research was supported by the Italian Ministry of University and Research, P.R.I.N. 2015, project 2015JW9NJT Advanced mechanical modeling of new materials and structures for the solution of 2020 Horizon challenges, Sapienza Research Unit (grant B86J16002300001) by Sapienza University, grant 2016 (B82F16005920005), and P.R.I.N. 2017 no. 20172017HF PKZY (cup: B86J16002300001).

REFERENCES

Addessi, D. and Sacco, E., A Multi-Scale Enriched Model for the Analysis of Masonry Panels, *Int. J. Solids Struct.*, vol. **49**, no. 6, pp. 865–880, 2012.

- Alibert, J.J. and Della Corte, A., Second-Gradient Continua as Homogenized Limit of Pantographic Microstructured Plates: A Rigorous Proof, *Z. Angew. Math. Phys.*, vol. **66**, no. 5, pp. 2855–2870, 2015. DOI: 10.1007/s00033-015-0526-x
- Altenbach, H. and Sadowski, T., *Failure and Damage Analysis of Advanced Materials*, CISM International Centre for Mechanical Sciences, Vienna, Austria: Springer, 2014.
- Bacca, M., Bigoni, D., Corso, F.D., and Veber, D., Mindlin Second-Gradient Elastic Properties from Dilute Two-Phase Cauchy-Elastic Composites. Part I: Closed Form Expression for the Effective Higher-Order Constitutive Tensor, *Int. J. Solids Struct.*, vol. **50**, no. 24, pp. 4010–4019, 2013.
- Bacigalupo, A. and Gambarotta, L., Second-Order Computational Homogenization of Heterogeneous Materials with Periodic Microstructure, *ZAMM – J. Appl. Math. Mech./Z. Angew. Math. Mech.*, vol. **90**, nos. 10–11, pp. 796–811, 2010.
- Baraldi, D., Reccia, E., and Cecchi, A., In Plane Loaded Masonry Walls: DEM and FEM/DEM Models. A Critical Review, *Meccanica*, vol. **53**, pp. 1613–1628, 2018.
- Bouyge, F., Jasiuk, I., and Ostoja-Starzewski, M., A Micromechanically based Couplestress Model of an Elastic Two-Phase Composite, *Int. J. Solids Struct.*, vol. **38**, no. 10, pp. 1721–1735, 2001.
- Budiansky, B., On the Elastic Moduli of Some Heterogeneous Materials, *J. Mech. Phys. Solids*, vol. **13**, no. 4, pp. 223–227, 1965.
- Civalek, O., Demir, C., and Akgöz, B., Free Vibration and Bending Analyses of Cantilever Microtubules based on Nonlocal Continuum Model, *Math. Comput. Appl.*, vol. **15**, no. 2, pp. 289–298, 2010.
- Demir, C. and Civalek, O., Torsional and Longitudinal Frequency and Wave Response of Microtubules based on the Nonlocal Continuum and Nonlocal Discrete Models, *Appl. Math. Model.*, vol. **37**, no. 22, pp. 9355–9367, 2013.
- Drugan, W. and Willis, J., A Micromechanics-Based Nonlocal Constitutive Equation and Estimates of Representative Volume Element Size for Elastic Composites, *J. Mech. Phys. Solids*, vol. **44**, no. 4, pp. 497–524, 1996.
- Ehlers, W., *Recovering Micropolar Continua from Particle Mechanics by Use of Homogenisation Strategies*, Berlin: Springer, pp. 179–189, 2011.
- Eremeyev, V.A. and Pietraszkiewicz, W., Material Symmetry Group and Constitutive Equations of Micropolar Anisotropic Elastic Solids, *Math. Mech. Solids*, vol. **21**, no. 2, pp. 210–221, 2016. DOI: 10.1177/1081286515582862
- Fantuzzi, N., Leonetti, L., Trovalusci, P., and Tornabene, F., Some Novel Numerical Applications of Cosserat Continua, *Int. J. Comput. Methods*, vol. **15**, no. 6, p. 1850054, 2018. DOI: 10.1142/S0219876218500548
- Fantuzzi, N., Trovalusci, P., and Dharasura, S., Mechanical Behavior of Anisotropic Composite Materials as Micropolar Continua, *Front. Mater.*, vol. **6**, no. 1, p. 59, 2019.
- Favata, A., Trovalusci, P., and Masiani, R., A Multiphysics and Multiscale Approach for Modeling Microcracked Thermo-Elastic Materials, *Comput. Mater. Sci.*, vol. **116**, pp. 22–31, 2016.
- Ferreira, A., *MATLAB Codes for Finite Element Analysis: Solids and Structures*, Solid Mechanics and Its Applications, The Netherlands: Springer, 2008.
- Forest, S., Dendievel, R., and Canova, G.R., Estimating the Overall Properties of Heterogeneous Cosserat Materials, *Model. Simul. Mater. Sci. Eng.*, vol. **7**, no. 5, pp. 829–840, 1999. DOI: 10.1088/2F0965-0393/2F7%2F5%2F314
- Forest, S., Pradel, F., and Sab, K., Asymptotic Analysis of Heterogeneous Cosserat Media, *Int. J. Solids Struct.*, vol. **38**, no. 26, pp. 4585–4608, 2001.
- Forest, S. and Sab, K., Cosserat Overall Modeling of Heterogeneous Materials, *Mech. Res. Commun.*, vol. **25**, no. 4, pp. 449–454, 1998.
- Greco, F., Leonetti, L., Luciano, R., and Blasi, P.N., Effects of Microfracture and Contact Induced Instabilities on the Macroscopic Response of Finitely Deformed Elastic Composites, *Compos. Part B: Eng.*, vol. **107**, pp. 233–253, 2016.
- Greco, F., Leonetti, L., Luciano, R., and Trovalusci, P., Multiscale Failure Analysis of Periodic Masonry Structures with Traditional and Fiber-Reinforced Mortar Joints, *Compos. Part B: Eng.*, vol. **118**, pp. 75–95, 2017.
- Greco, F., Leonetti, L., Medaglia, C.M., Penna, R., and Pranno, A., Nonlinear Compressive Failure Analysis of Biaxially Loaded Fiber Reinforced Materials, *Compos. Part B: Eng.*, vol. **147**, pp. 240–251, 2018.
- Jain, J.R. and Ghosh, S., Damage Evolution in Composites with a Homogenization-Based Continuum Damage Mechanics Model, *Int. J. Damage Mechan.*, vol. **18**, no. 6, pp. 533–568, 2009. DOI: 10.1177/1056789508091563
- Kouznetsova, V., Geers, M., and Brekelmans, W., Multi-Scale Second-Order Computational Homogenization of Multi-Phase Materials: A Nested Finite Element Solution Strategy, *Comput. Methods Appl. Mech. Eng.*, vol. **193**, no. 48, pp. 5525–5550, 2004.

- Kouznetsova, V., Geers, M.G.D., and Brekelmans, W.A.M., Multi-Scale Constitutive Modelling of Heterogeneous Materials with a Gradient-Enhanced Computational Homogenization Scheme, *Int. J. Numer. Methods Eng.*, vol. **54**, no. 8, pp. 1235–1260, 2002.
- Kunin, I.A., The Theory of Elastic Media with Microstructure and the Theory of Dislocations, in *Mechanics of Generalized Continua*, E. Kröner, Ed., Berlin: Springer, pp. 321–329, 1968.
- Larsson, R. and Zhang, Y., Homogenization of Microsystem Interconnects based on Micropolar Theory and Discontinuous Kinematics, *J. Mech. Phys. Solids*, vol. **55**, no. 4, pp. 819–841, 2007.
- Leismann, T. and Mahnken, R., Comparison of Hyperelastic Micromorphic, Micropolar and Microstrain Continua, *Int. J. Non-Linear Mech.*, vol. **77**, pp. 115–127, 2015.
- Leonetti, L., Fantuzzi, N., Trovalusci, P., and Tornabene, F., Scale Effects in Orthotropic Composite Assemblies as Micropolar Continua: A Comparison between Weak- and Strong-Form Finite Element Solutions, *Materials*, vol. **12**, no. 5, 2019.
- Luciano, R. and Willis, J., Bounds on Non-Local Effective Relations for Random Composites Loaded by Configuration-Dependent Body Force, *J. Mech. Phys. Solids*, vol. **48**, no. 9, pp. 1827–1849, 2000.
- Masiani, R. and Trovalusci, P., Cosserat and Cauchy Materials as Continuum Models of Brick Masonry, *Meccanica*, vol. **31**, no. 4, pp. 421–432, 1996. DOI: 10.1007/BF00429930
- Massart, T.J., Peerlings, R.H.J., and Geers, M.G.D., An Enhanced Multi-Scale Approach for Masonry Wall Computations with Localization of Damage, *Int. J. Numer. Methods Eng.*, vol. **69**, no. 5, pp. 1022–1059, 2007.
- Nemat-Nasser, S., Hori, M., and Achenbach, J., *Micromechanics: Overall Properties of Heterogeneous Materials*, Amsterdam: Elsevier Science, 2013.
- Nguyen, V.P., Lloberas-Valls, O., Stroeve, M., and Sluys, L.J., Computational Homogenization for Multiscale Crack Modeling. Implementational and Computational Aspects, *Int. J. Numer. Methods Eng.*, vol. **89**, no. 2, pp. 192–226, 2012.
- Onck, P.R., Cosserat Modeling of Cellular Solids, *Comptes Rendus Mécanique*, vol. **330**, no. 11, pp. 717–722, 2002.
- Ostoja-Starzewski, M., Boccarda, S.D., and Jasiuk, I., Couple-Stress Moduli and Characteristics Length of a Two-Phase Composite, *Mech. Res. Commun.*, vol. **26**, no. 4, pp. 387–396, 1999.
- Pau, A. and Trovalusci, P., Block Masonry as Equivalent Micropolar Continua: The Role of Relative Rotations, *Acta Mech.*, vol. **223**, no. 7, pp. 1455–1471, 2012. DOI: 10.1007/s00707-012-0662-8
- Peerlings, R.H.J. and Fleck, N.A., Computational Evaluation of Strain Gradient Elasticity Constants, *Int. J. Multiscale Comput. Eng.*, vol. **2**, no. 4, 2004.
- Reccia, E., Leonetti, L., Trovalusci, P., and Cecchi, A., A Multiscale/Multidomain Model for the Failure Analysis of Masonry Walls: A Validation with a Combined FEM/DEM Approach, *Int. J. Multiscale Comput. Eng.*, vol. **16**, pp. 325–343, 2018.
- Reddy, J., *Introduction to the Finite Element Method*, New York: McGraw-Hill, 2004.
- Reddy, J., *Energy Principles and Variational Methods in Applied Mechanics*, New York: Wiley, 2017.
- Rizzi, G., Corso, F.D., Veber, D., and Bigoni, D., Identification of Second-Gradient Elastic Materials from Planar Hexagonal Lattices. Part II: Mechanical Characteristics and Model Validation, *Int. J. Solids Struct.*, vols. **176–177**, pp. 19–35, 2019.
- Scherphuis, J., Jaap's Puzzle Page, accessed on September 19, 2019 from <http://www.jaapsch.net/tilings>, 2019.
- Sluys, L., de Borst, R., and Mühlhaus, H.B., Wave Propagation, Localization and Dispersion in a Gradient-Dependent Medium, *Int. J. Solids Struct.*, vol. **30**, no. 9, pp. 1153–1171, 1993.
- Smyshlyaev, V. and Cherednichenko, K., On Rigorous Derivation of Strain Gradient Effects in the Overall Behaviour of Periodic Heterogeneous Media, *J. Mech. Phys. Solids*, vol. **48**, no. 6, pp. 1325–1357, 2000.
- Sokolowski, M., *Theory of Couple-Stresses in Bodies with Constrained Rotations*, Vol. 26 of *CISM Courses and Lectures*, Vienna, Austria: Springer, 1972.
- Tekolu, C. and Onck, P.R., Size Effects in Two-Dimensional Voronoi Foams: A Comparison between Generalized Continua and Discrete Models, *J. Mech. Phys. Solids*, vol. **56**, no. 12, pp. 3541–3564, 2008.
- Trovalusci, P., *Molecular Approaches for Multifield Continua: Origins and Current Developments*, Vienna, Austria: Springer, pp. 211–278, 2014. DOI: 10.1007/978-3-7091-1812-2_7
- Trovalusci, P., Bellis, M.L.D., and Masiani, R., A Multiscale Description of Particle Composites: From Lattice Microstructures to Micropolar Continua, *Compos. Part B: Eng.*, vol. **128**, pp. 164–173, 2017.

- Trovalusci, P. and Masiani, R., Material Symmetries of Micropolar Continua Equivalent to Lattices, *Int. J. Solids Struct.*, vol. **36**, no. 14, pp. 2091–2108, 1999.
- Trovalusci, P. and Masiani, R., Non-Linear Micropolar and Classical Continua for Anisotropic Discontinuous Materials, *Int. J. Solids Struct.*, vol. **40**, no. 5, pp. 1281–1297, 2003.
- Trovalusci, P. and Masiani, R., A Multifield Model for Blocky Materials based on Multiscale Description, *Int. J. Solids Struct.*, vol. **42**, no. 21, pp. 5778–5794, 2005.
- Trovalusci, P. and Pau, A., Derivation of Microstructured Continua from Lattice Systems via Principle of Virtual Works: The Case of Masonry-Like Materials as Micropolar, Second Gradient and Classical Continua, *Acta Mech.*, vol. **225**, no. 1, pp. 157–177, 2014.
- Trovalusci, P. and Sansalone, V., A Numerical Investigation of Structure-Property Relations in Fiber Composite Materials, *Int. J. Multisc. Comput. Eng.*, vol. **5**, no. 2, pp. 141–152, 2007.
- Trovalusci, P., Varano, V., and Rega, G., A Generalized Continuum Formulation for Composite Microcracked Materials and Wave Propagation in a Bar, *J. Appl. Mech.*, vol. **77**, no. 6, p. 061002, 2010. DOI: 10.1115/1.4001639
- Tuna, M., Kirca, M., and Trovalusci, P., Deformation of Atomic Models and Their Equivalent Continuum Counterparts Using Eringens Two-Phase Local/Nonlocal Model, *Mech. Res. Commun.*, vol. **97**, pp. 26–32, 2019.
- Tuna, M. and Trovalusci, P., Scale Dependent Continuum Approaches for Discontinuous Assemblies: Explicit and Implicit Non-Local Models, *Mech. Res. Commun.*, vol. **103**, p. 103461, 2020. DOI: 10.1016/j.mechrescom.2019.103461
- Yang, D., Sheng, Y., Ye, J., and Tan, Y., Collapse Behaviour of Three-Dimensional Brick-Block Systems Using Non-Linear Programming, *Struct. Eng. Mech.*, vol. **10**, no. 2, pp. 181–195, 2000.
- Yang, D., Sheng, Y., Ye, J., and Tan, Y., Discrete Element Modeling of the Microbond Test of Fiber Reinforced Composite, *Comput. Mater. Sci.*, vol. **49**, no. 2, pp. 253–259, 2010.